Publications of the Astronomical Society of the Pacific, 129:055002 (13pp), 2017 May https://doi.org/10.1088/1538-3873/aa60b5

Ground-based Observation System Development for the Moon Hyper-spectral Imaging

Yang Wang[1,2], Yu Huang[1], Shurong Wang[1], Zhanfeng Li[1], Zihui Zhang[1], Xiuqing Hu[3], and Peng Zhang[3]
[1] Changchun Institute of Optics, Fine Mechanics and Physics, Chinese Academy of Sciences, China
[2] University of Chinese Academy of Sciences, China
[3] National Satellite Meteorological Center, China; huxq@cma.gov.cn
Received 2016 December 5; accepted 2017 January 20; published 2017 March 31

Abstract

The Moon provides a suitable radiance source for on-orbit calibration of space-borne optical instruments. A ground-based observation system dedicated to the hyper-spectral radiometry of the Moon has been developed for improving and validating the current lunar model. The observation instrument using a dispersive imaging spectrometer is particularly designed for high-accuracy observations of the lunar radiance. The simulation and analysis of the push-broom mechanism is made in detail for lunar observations, and the automated tracking and scanning is well accomplished in different observational condition. A three-month series of hyper-spectral imaging experiments of the Moon have been performed in the wavelength range from 400 to 1000 nm near Lijiang Observatory (Yunnan, China) at phase angles −83°–87°. Preliminary results and data comparison are presented, and it shows the instrument performance and lunar observation capability of this system are well validated. Beyond previous measurements, this observation system provides the entire lunar disk images of continuous spectral coverage by adopting the push-broom mode with special scanning scheme and leads to the further research of lunar photometric model.

Key words: instrumentation: spectrographs – methods: observational – Moon – techniques: imaging spectroscopy – techniques: photometric

Online material: color figures

1. Introduction

In the harsh space environment, the radiometric response of the optical instruments often changes with time in an unpredictable and unknown fashion. The reliable calibration methods will be used across the Earth Observing System to provide traceability to absolute standards and inter-mission calibration with high accuracy. A standard reference source using the Moon is established to provide on-orbit stable and accurate radiometric calibration of weather and climate remote-sensing instruments in solar reflective wavelength range (Ohring et al. 2005, 2007).

The Moon has several advantages for being used as a calibration target for satellite instruments, and lunar-based calibration is very complementary to other current vicarious calibration methods. The reflectance properties of the Moon's surface are photometrically stable (10^{-8} per year) (Kieffer 1997), and the Moon is accessible for all spacecraft regardless of orbit. Lunar brightness has a dynamic range for most Earth-observing spacecraft instruments (Kieffer & Anderson 1998). During the lunar calibration for space-borne instruments, the Moon not only can be directly observed using instrument's normal Earth-observing optical path without restriction, but also it is not affected by the atmosphere. Careful visible NIR characterization of the Moon as an absolute radiometric standard with phase angle provides common calibration for multiple instruments, even ones that operate at different times (Kieffer & Stone 2005).

However, the major difficulty using the Moon as an ideal target for radiometric calibration is that the actual photometric model of the Moon is not very accurate, owing to complex photometric behavior and non-uniform reflectance on the lunar surface (Kieffer & Anderson 1998). The photometric model is based on a large number of lunar measurements, including on-orbit and ground-based observations. When obtaining the absolute radiances from lunar images, the controllability of ground-based observations is much better than that of space-craft observations, even though the observations are disturbed by the atmosphere. The advantage of ground-based observations is that we can compare the obtained data with those of other instruments. There have been several ground-based lunar photometric observations and lunar irradiance models, and these include the following:

(1). During 1964–1965, the earliest photoelectric observations of the Moon covering phase angles 6°–120° have

been made in nine narrow bands between 359 and 1064 nm and the *UBV* by Lane & Irvine (1973). Miller–Turner has developed a lunar irradiance model for quantifying the top-of-atmosphere hyper-spectral irradiance by incorporating solar source observation, lunar spectral albedo data and phase functions derived from Lane and Irvine (Miller & Turner 2009).

(2). To date, the most comprehensive radiometric study of the Moon is based on a database of spatially resolved radiance images acquired from the USGS's Robotic Lunar Observatory (ROLO) from 1996 to 2003. The observational data has been collected in 32 bands from 350 to 2450 nm, and a wide range of libration angles, phase angles from near eclipse to typically 90°. The most frequently used lunar photometric model is based on a data set of radiance measurements acquired by the ROLO (Kieffer & Wildey 1996; Kieffer & Stone 2005).

(3). Kazuto Saiki et al. (2008) use a tunable liquid-crystal filter (LCTF) telescope to acquire multi-band images (five bands: 650, 750, 900, 950, and 1000 nm) of the lunar surface at a phase angle near 7°. The quasi-simultaneous imaging photometric observations of the Moon and the Sun, which use a CMOS-camera Canon EOS 300D in three spectral bands (R: 603 nm, G: 529 nm, and B: 472 nm), have been carried out in a wide range of phase angles (1°.6–168°) in 2006 August–October (Velikodsky et al. 2011).

(4). The ground-based radiometric measurements of the Moon using a Schmidt–Cassegrain telescope and a field spectroradiometer covering wavelengths from 400 to 2500 nm have been performed at phase angle 23° (Lawrence et al. 2003). Another measurement of lunar spectral irradiance from 420 to 1000 nm which uses a non-imaging spectrograph is reported with lunar phase ranging from 17° to 20° (Smith et al. 2012; Cramer et al. 2013a, 2013b).

The lunar observations within the past 10 years have been made with various on-orbit explorers (Sun et al. 2007; Besse et al. 2013; Ohtake et al. 2013; Pieters et al. 2013), such as the Spectral Profiler, the Multiband Imager, the Terrain Camera onboard the *SELENE* mission, the Moon Mineralogy Mapper onboard the *Chandrayaan*-1 mission and the Solar-Stellar Irradiance Comparison Experiment on board the *Solar Radiation and Climate Experiment* (Butler et al. 2007), have provided extensive data covering the UV, VIS and NIR spectral range.

The irradiance model has been used to determine long-term degradation in the radiometric response of satellite sensors (Barnes et al. 2004; Kieffer & Stone 2005), and provides a technique for the cross calibration of instruments (Jr et al. 2011). The improvement of radiometric models can be applied retroactively to instrument calibration in the future. Furthermore, lunar observations can provide nighttime measurements to complement aerosol data when the Sun is not available (Berkoff et al. 2011; Barreto et al. 2013), and the nighttime low-light measurements from the Night Band in the satellite require the accurate spectral irradiance from the lunar model (Miller & Turner 2009).

The dispersive imaging spectroscopy of our observation system has been widely applied to many hyper-spectral imagers, which provides spatial and spectral information related to observed target. The radiometric observations of the entire lunar disk using an imaging spectrometer were made near Lijiang observatory, Yunnan Province from 2015 December to 2016 February. Section 2 describes this observation system and its components, particularly the imaging spectrometer. In Section 3, this paper presents details of the Moon's scanning mode and automated observations, and its simulation results show that the scheme design is valid. Section 4 gives a description of experimental observations of the Moon. The preliminary results and relative comparison of ground-based lunar photometric observations are addressed in Section 4.

2. Instrumentation

The ground-based observation system mainly includes an imaging spectrometer, an equatorial mount and an imaging monitor (see Figure 1). The imaging spectrometer together with the imaging monitor is fixed on the equatorial mount with a tripod. The imaging monitor is rigidly fixed to the imaging spectrometer, and the optical axis parallelism between the imaging monitor and the imaging spectrometer should be kept. The imaging spectrometer is set on a versa-plate to make a slit parallel to the versa-plate so that the spectrometer slit is exactly perpendicular to the Moon's movement trail.

2.1. Imaging Spectrometer

In order to meet the needs of the Moon hyper-spectral imaging, the spectrometer is designed to be a prism dispersion instrument with the slit. The optical design and layout of the instrument are shown in Figure 2, in which optical components are labeled. The ground-based imaging spectrometer consists of the fore-telescope system and the spectrometer optical dispersive system. They can perfectly satisfy the relative aperture matching principle. The fore-telescope is designed to be a refraction optical system, and the spectrometer is mainly designed to be a reflective optical system. The spectrometer system with reflecting refractive prismatic dispersion is composed of a slit, a reflection mirror, collimating lenses and imaging lenses, and one cooled Charge-coupled Device (CCD) detector.

The light from the Moon passes through the fore-telescope system and focuses onto the entrance slit which is fully filled with light. The imaging spectrometer utilizes the slit to limit the

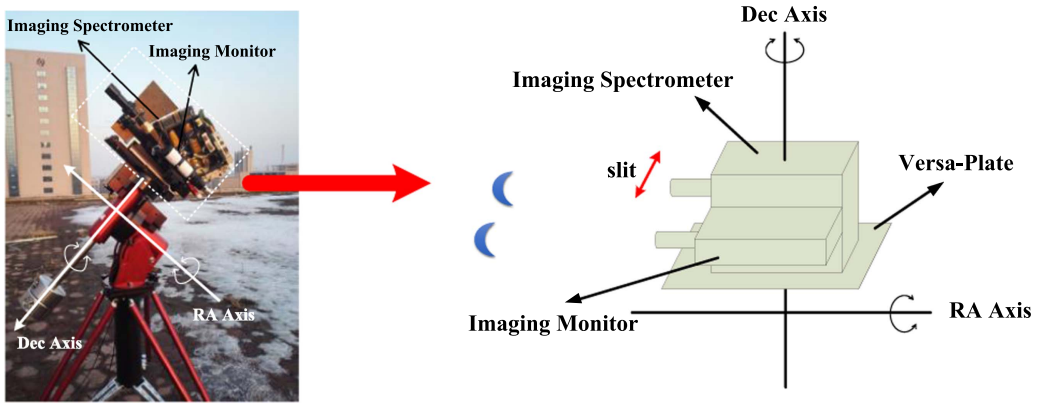

Figure 1. Structure chart of the ground-based photometric observation system (Left: instrument photo; Right: schematic diagram).
(A color version of this figure is available in the online journal.)

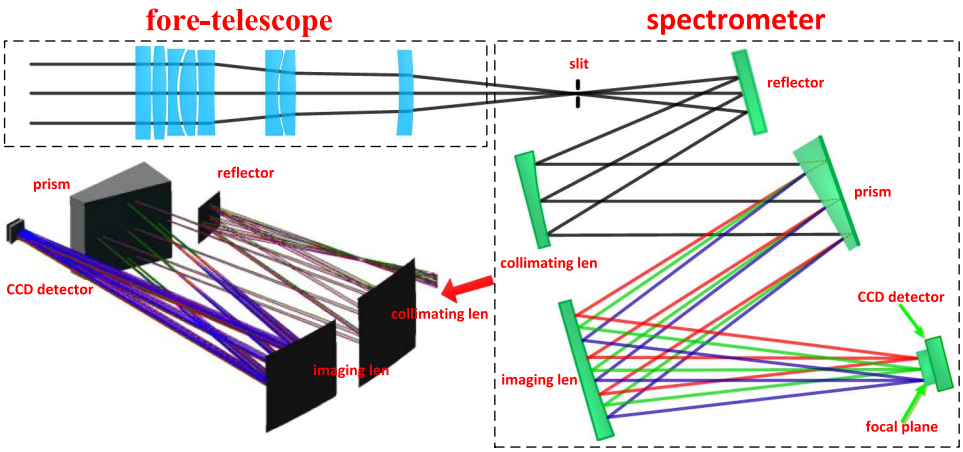

Figure 2. Layout of the Moon imaging spectrometer. The imaging spectrometer consists of the fore-telescope system and the spectrometer system.
(A color version of this figure is available in the online journal.)

field-of-view of the instrument. The light from the slit is collimated by the collimating lens and then dispersed through the prism, and finally the dispersed image of the slit is produced onto the focal plane of imaging lens. The effective area of 253 spatial columns and 273 spectral rows is used in the center of the CCD detector arrays.

The imaging spectrometer physical specifications are given in Table 1. The optical system covers from the visible to near-infrared wavelength regions with a spectral resolution of 2–10 nm because of the nonlinear dispersion of prism material. The spatial resolution of the imaging spectrometer is 38 km × 20 km on the surface of the Moon. The signal-to-noise ratio (S/N) of the Moon imaging spectrometer at brightness level of full Moon is shown in Figure 3. The S/N is more than 200 except for the wavelength from 400 to

Table 1
Imaging Spectrometer Physical Specifications

Instrument	Specification	Remakes
Spectral range	400–1000 nm	Single CCD
Spectral channels	>270	Electronically selectable
Spectral sampling width	2–10 nm	Nonlinear dispersion
Sampling interval	(0.34–0.57) × Sampling width	Nonlinear dispersion
Field of view (FOV)	0°7	Across track
Instantaneous Field of view (IFOV)	0°0056	Along track
Pixels across track	253	…
Dynamic Range	10^6	…
Focus length	256.4 mm	…
S/N	See in Figure 3	400–1000 nm

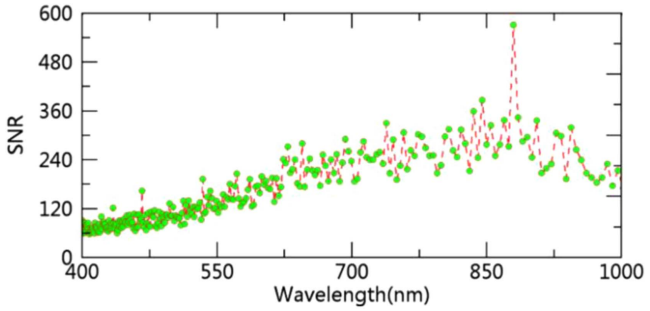

Figure 3. S/N of the Moon imaging spectrometer at the near full Moon. (A color version of this figure is available in the online journal.)

600 nm, which is good enough for lunar radiance observations.

2.2. Equatorial Mount

The paramount MX+ Robotic Telescope Mount is an ultra-precision German equatorial mount that is designed to deliver unmatched pointing, tracking and stability in portable or permanent installations. Integrated USB 2.0 computer to mount communication interface can be controlled via the Sky X Professional Edition. After calibrated azimuth and elevation polar alignment adjustments, 30″ of pointing accuracy in all sky is obtained by using interactive telescope pointing analysis software. The equatorial mount has a maximum 7″ tracking periodic error (peak-to-peak) without periodic error correction. If the periodic error is corrected, the final peak-to-peak error should be about 1″ or less. A common equatorial mounting plate that can accept most of telescopes or standard paramount MX+ wedges can be adjusted to reach the latitude from 10° to 65°.

Parallel to the axis of the polar axis is called as "R.A. axis," and the other axis of rotation on the equatorial plane of the celestial sphere is called as "decl. axis." The maximum slew and tracking speed is 6° per second in both R.A. axis and decl. axis. The rotation of the Earth is offset by the tracking of the RA axis. This kind of equatorial mount coordinate system is not only relatively easy to operate the mount, but also suitable for automated observations for long term. Therefore, the accurate tracking and pointing of the Moon in the nighttime sky are provided by the paramount MX+ Robotic Telescope Mount.

2.3. Imaging Monitor

The imaging monitor is mainly composed of an astronomical telescope and a CMOS detector. The telescope is manufactured by SKY ROVER, whose aperture is 50 mm and focal length is 218 mm. The size of the CMOS-matrix is 1024 × 1280 pixels, and a QHY 5-II is used as the imaging detector of the Moon, which allows us to obtain the images of the full lunar disk. At the same time, the imaging monitor can be utilized to align the equatorial mount's polar axis with the celestial pole. Before automated observations, the imaging monitor can be used for positing the Moon in the field of view of the imaging spectrometer. In addition, the lunar images from the imaging monitor are also used for checking the hyper-spectral images from the imaging spectrometer and helping post-processing such as the Moon image correction or matching.

Before the data acquisition, several related parameters, including observation location, humidity, and atmospheric pressure, are put into the observation and control system on the master computer which is also connected to the network for accurate clock synchronization. To improve the mount's pointing performance, the calibration of the polar alignment need to be performed before the experiment. At the beginning of each night of lunar observations, the integration times of the instruments, including the imaging spectrometer and the imaging monitor, should be set to match the lunar brightness. Although most of the instrument operations are conducted automatically, an operator has to be on duty for monitoring the instrument operation.

3. Scanning Method and Automated Observations of the Moon

3.1. Scanning Mode

The hyper-spectral imaging data of the Moon is obtained by the slit imaging and continuous scanning with the imaging spectrometer. In the process of tracking the Moon, the imaging spectrometer requires a high tracking and pointing accuracy of the tracking system for push-broom imaging. To avoid this, the ground-based observational data is obtained by scanning the Moon while parking the spectrometer as the Moon moves across the field of view. As the Moon moves, the view plane of the imaging spectrometer sweeps a region of the Moon at regular intervals, and one-dimensional images of the view plane are captured. A two-dimensional image is obtained by the ensemble of these images. Push-broom imaging spectrometer is mounted on the equatorial telescope, and the direction of the length of the slit is perpendicular to the direction of the Moon's apparent motion.

3.1.1. Angular Velocity of the Moon

During the observation night, the apparent motion of the Moon is similar to a parabolic curve at which the angular velocity changes with time, and the orientation of the Moon is not same during one night. The simulation-based testing depends on some parameters of the Moon motion trajectory, which are based upon the Moon position algorithm. The Solar and Moon Position Algorithm (SAMPA) distributed by the National Renewable Energy Laboratory is used, which calculates the solar and lunar zenith angle and azimuth angle based upon the date, time, site and so on.

In Figure 4, x axis direction is the Earth's north, y axis direction is the Earth's east and z axis points to the zenith, θ_1, θ_2

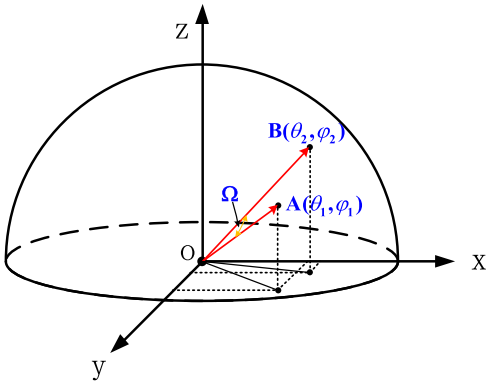

Figure 4. Moon position relationship between two points in the time interval ΔT_0.
(A color version of this figure is available in the online journal.)

are the lunar zenith angle in point A and B, respectively, φ_1, φ_2 are the lunar azimuth angle in point A and B, respectively. The vector ***OA*** and ***OB*** in the horizontal coordinate system, respectively, are

$$\boldsymbol{OA} = [\sin(\theta_1)\sin(\varphi_1), \sin(\theta_1)\cos(\varphi_1), \cos(\theta_1)]R_A, \quad (1)$$

$$\boldsymbol{OB} = [\sin(\theta_2)\sin(\varphi_2), \sin(\theta_2)\cos(\varphi_2), \cos(\theta_2)]R_B, \quad (2)$$

where R is the distance between the Moon and the observation site, and R_A is approximately equal to R_B within the time ΔT_0, which is a time interval from point A to point B. The angle ψ between straight line OA and OB is evaluated by

$$\cos(\psi) = \frac{\boldsymbol{OA} \cdot \boldsymbol{OB}}{|\boldsymbol{OA}| \times |\boldsymbol{OB}|}. \quad (3)$$

It is assumed that the angular velocity is a constant within the time ΔT_0, and the angular velocity ω_{track} of the Moon with respect to the instrument coordinate system is

$$\psi = \Delta T_0 \times \omega_{track} \quad (4)$$

$$\omega_{track} = \frac{1}{\Delta T_0}\cos^{-1}[\sin(\theta_1)\cos(\varphi_1)\sin(\theta_2)\cos(\varphi_2) + \sin(\theta_1)\sin(\theta_2)\sin(\varphi_1)\sin(\varphi_2) + \cos(\theta_1)\cos(\theta_2)]. \quad (5)$$

In Equations (4) and (5), ΔT_0 is a small value, and we can set ΔT_0 equal to 20 s. The angular velocity ω_{track} calculated by Equations (1)–(5) with respect to the observation site at time T is obtained in the way that the angular distance ψ of the Moon motion within the period of ΔT_0 is calculated by lunar zenith and azimuth angles at time $(T - \Delta T_0/2)$ and $(T + \Delta T_0/2)$.

3.1.2. Variation of the Angular Velocity within One Lunar Disk

To validate the feasibility of the Moon's scanning mode, motion trajectory is simulated during one full lunar disk. In the direction of motion, a time interval of one full lunar disk is

$$T_{disk} = \frac{\psi_{moon}}{\omega_{track}}, \quad (6)$$

where ψ_{moon} is the apparent angular diameter of the Moon with respect to the observation site, $\psi_{moon} \approx 0.^{\circ}5$ and the time of the Moon passing through the spectrometer slit is T_{disk} (about 130 s during a lunar observation). The assumption that T_{disk} is equal to 130 s is made in the discussion below.

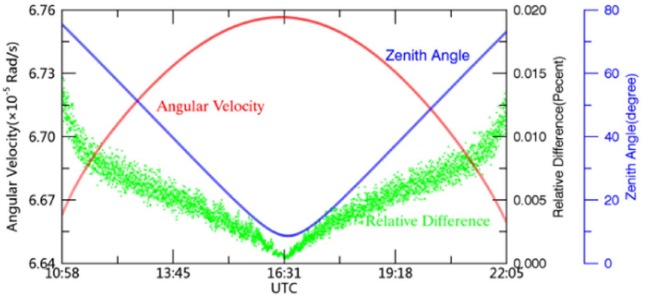

Figure 5. Variation of the angular velocity within one lunar disk.
(A color version of this figure is available in the online journal.)

In Figure 5, the blue line shows the zenith angle ranges from rise time to set time on 2015 December 23, and the red line shows the angular velocity ω_{track} with time. For time$T$, the maximum absolute value RD(T) of the relative differences in the angular velocity during the acquisition of one lunar disk is

$$\mathrm{RD}(T) = \frac{\max(|\omega_{track}(t) - \omega_{track}(T)|)}{\omega_{track}(T)}, \quad t \in \left(T - \frac{T_{disk}}{2}, T + \frac{T_{disk}}{2}\right), \quad (7)$$

where time t ranges from $T - T_{disk}/2$ to $T + T_{disk}/2$ during the acquisition of one lunar disk, and the time T (x-axis) is the middle time of one lunar disk. In Figure 5, the light green scattered points show the maximum absolute value $RD(T)$ of the relative difference of the angular velocity with time T. The angular velocity of the Moon is constantly changing and the greatest near the smallest zenith angle location. The variation in the angular velocity within one lunar disk can be negligible, even though RD(T) is the maximum value (approximately 0.015%) at the zenith angle of 73°.

3.1.3. Linearity of the Motion Path within One Lunar Disk

When the mount slews to the Moon, the spectrometer slit is perpendicular to the direction of the lunar apparent motion. The Moon position with time during one night on 2015 December 24 is illustrated in Figure 6(1), and the motion trail of the Moon is a curve in one night. The following analysis about the trajectory linearity is made within one lunar disk.

In Figure 6(1), the red line in the horizontal coordinate system shows the Moon position with time, and the Moon

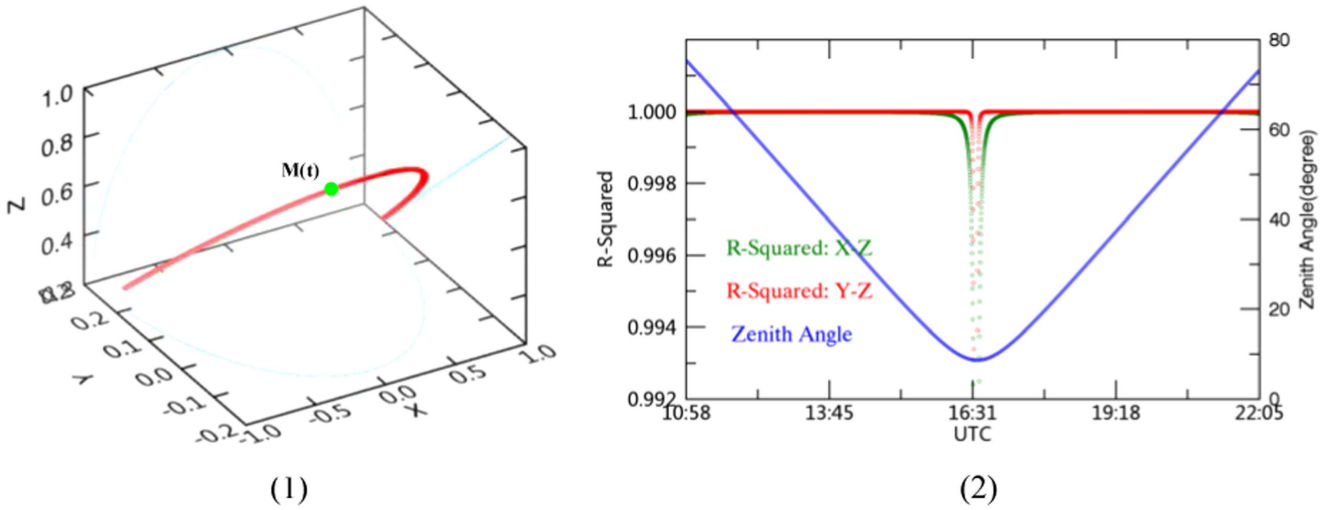

Figure 6. Linearity of the movement path within one lunar disk.
(A color version of this figure is available in the online journal.)

position $M(t)$ is expressed as

$$M(t) = [M_x(t), M_y(t), M_z(t)]. \quad (8)$$

The components of the Moon position $M(t)$ related to x axis, y axis and z axis, respectively, are

$$\begin{aligned} M_z(t) &= \sin(\theta)\sin(\varphi)R(t), \\ M_z(t) &= \sin(\theta)\cos(\varphi)R(t), \\ M_z(t) &= \cos(\theta)R(t), \end{aligned} \quad (9)$$

where $R(t)$ is the distance from the Moon to the observing site. An assumption is made that $R(t)$ is approximately equal to a value R_0 in one night, and R_0 is used as 1 unit in Figure 6(1). The zenith angle θ and the azimuth angle φ, respectively, are a function of time t. Both of Figures 4 and 6(1) have the same coordinate system, and the Moon position $M(t)$ at time t in Figure 6(1) may be A or B point in Figure 4. Light blue lines show the Moon position $M(t)$ is projected on x–y, x–z and y–z coordinate plane.

The R-Square $R^2_{x-z}(T)$ and $R^2_{y-z}(T)$ of a linear regression in x–z direction and y–z direction in Figure 6(2), which is the best-fit line of $M_z(t)$ with respect to $M_x(t)$ and $M_y(t)$ within the period of $T_{\rm disk}$, respectively, are given by

$$\begin{aligned} R^2_{x-z}(T), R^2_{y-z}(T) \longleftarrow M_z(t) &= aM_x(t) + bM_y(t) + c \\ t \in \left(T - \frac{T_{\rm disk}}{2}, T + \frac{T_{\rm disk}}{2}\right), \end{aligned} \quad (10)$$

where a, b, and c are the linear fitting coefficients in a plane within one lunar disk in the horizontal coordinate system.

During one lunar disk, the movement trajectory $M(t)$ of the Moon and the R-square for the best-fit line of $M(t)$, respectively, are shown in Figures 6(1) and (2). The Earth's rotation and the Moon's revolution can be included in the apparent motion of the Moon, and the composite motion can be considered to be rectilinear at one lunar disk interval. For one lunar disk, linear goodness of fit of the Moon motion trajectory with time is almost more than 99.8% in x–z direction and y–z direction (see Figure 6(2)), so the rotation of the Moon motion trajectory with respect to the observation site can be ignored during one lunar disk. In the instrument coordinate system, the push-broom instrument can be modeled as a pin-hole camera moving along a linear trajectory in space with a constant velocity and a fixed orientation during one lunar disk (Gupta & Hartley 1994).

3.2. Automated Observations

The lunar observations are very important to be conducted automatically for long-term data acquisition. When the instrument is parked ahead of the Moon in the motion direction, the Moon passes through the spectrometer slit, and a panoramic mosaic of the Moon is obtained within the period of ΔT. Based on the Moon position prediction from the astronomical software at any moment, the apparent motion trajectory of the Moon is not a line, but it is well known in the nighttime sky. The spectrometer slit should be orthogonal to the motion trajectory of the Moon. When the angular velocity $\omega_{\rm track}$ is well known and is a constant within one lunar disk, the rotation angle $\Delta\psi$ $(=\Delta T\omega_{\rm track})$ of the spectrometer slit is decided by time offset ΔT before push-broom imaging. Since the computer clock time increases by $\Delta T/2$ s, the master computer has run the Sky X Professional Edition on the modified time. When the mount slews to the Moon, the instrument points to the area which is in front of the Moon along the track direction.

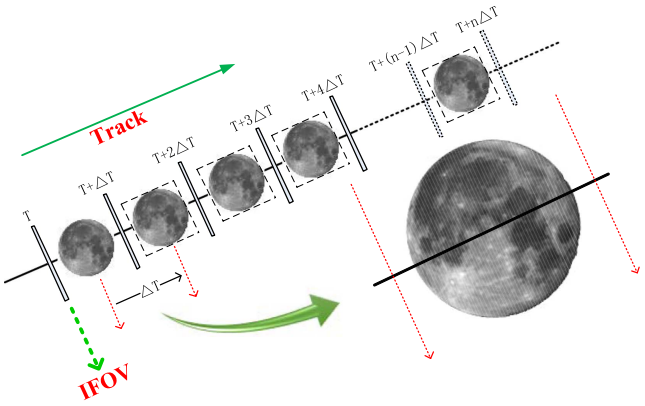

Figure 7. Working principle of automated observations for the imaging spectrometer.
(A color version of this figure is available in the online journal.)

3.2.1. Automated Process

The principle of automated observations for the imaging spectrometer is shown in Figure 7. T is the modified time of the master computer. A long rectangular box is the field of view of the instrument, and its position, which the imaging spectrometer starts to scan the Moon, is fixed in one night. The time interval of one complete lunar observation is

$$\Delta T = T_{\text{disk}} + T_{\text{space}} + \Delta T_{\text{slew}}, \tag{11}$$

where ΔT_{slew} is the setting time that the mount slew to the Moon, T_{space} is tolerance time for two sides of the Moon in the along-track direction.

When the mount slews to the Moon at time T, the master control system lets the imaging spectrometer gather data. After the mount has slewed to the correct coordinates of the Moon during a time period of ΔT_{slew}, the equatorial mount turns tracking off. The imaging spectrometer waits for the Moon sweeping through the spectrometer slit. The whole lunar disk of the imaging monitor and one frame slit image of the instrument are simultaneously obtained by the Moon motion with the instrument fixed. One lunar hyper-spectral imaging cube is well acquired within time $\Delta T - \Delta T_{\text{slew}}$. The instrument ends the data acquisition and slews to the next correct coordinates of the Moon at time $T + \Delta T$. The instrument starts to observe the next lunar disk, and then the nth lunar disk is automatically obtained to follow the steps above.

3.2.2. Tolerance Angle

For one full lunar disk, the tolerance angle $\Delta\psi_{\text{space}}$ along the track direction is

$$\Delta\psi_{\text{space}} = T_{\text{space}}\,\omega_{\text{track}}. \tag{12}$$

Equations (6) and (11) are applied in Equation (12) which becomes

$$\Delta\psi_{\text{space}} = \omega_{\text{track}}\,(\Delta T - \Delta T_{\text{slew}}) - \psi_{\text{moon}}. \tag{13}$$

Usually the time ΔT_{slew} is less than 2 s, so it is set to 2 s.

In order to capture the entire Moon and keep from long-playing tracking bias, the time interval ΔT of one lunar disk is greater than T_{disk}. The time T_{disk} ranges approximately from 120 to 140 s. When ΔT is equal to 180 s, the tolerance angle $\Delta\psi_{\text{space}}$ in Equation (13) is $0\overset{\circ}{.}18$–$0\overset{\circ}{.}24$ for the entire lunar disk in the along-track direction. The field of regard in the cross-track direction is $0\overset{\circ}{.}7$, which allows about $0\overset{\circ}{.}2$ tolerance for getting coverage of the entire full Moon. The spectrometer is able to capture all Moon phase observations, so this automated process is well-executed in one night.

3.2.3. Lunar Observation Time

The observing lunar zenith angle θ is determined by lunar zenith angle θ_{lunar} and solar zenith angle θ_{Sun}

$$\theta = (\theta_{\text{lunar}} < \theta_{\text{threshold}}) \| (\theta_{\text{Sun}} > 108^\circ), \tag{14}$$

where $\theta_{\text{threshold}}$ is the maximum zenith angle for lunar observations. When the solar zenith angle θ_{Sun} is more than 108°, the sky is in the twilight. The lunar observation time t_n is decided by the observing lunar zenith angle θ:

$$\theta \Rightarrow t_n \in [t_0,\, t_{\text{end}}], \tag{15}$$

$$t_n = T + n\Delta T \ (n = 0,\, 1,\, 2, \cdots, N), \tag{16}$$

where t_0 is the starting time for intraday observations, and t_{end} is the end time for intraday observations. The observing software use information, including the starting time and the end time, to decide how to observe the Moon. The starting time and the end time are decided together by evening and morning twilight of the Sun and the maximum zenith angle $\theta_{\text{threshold}}$ of the Moon. If the sky remains clear throughout the night, the process of observing the Moon continues until the time t_{end} is reached.

3.2.4. Oversampling Factor

The time T_{moon} of the instrument sweeping out one instantaneous field of view (IFOV) along the track direction is

$$T_{\text{moon}} = \frac{\psi_{\text{instantaneous}}}{\omega_{\text{track}}}, \tag{17}$$

where $\psi_{\text{instantaneous}}$ is the IFOV of the instrument, $\psi_{\text{instantaneous}} = 0\overset{\circ}{.}0056$, and the angular velocity of the Moon, ω_{track}, is calculated based on Equation (5). Determine the oversampling factor, normally presumed to be same for all bands. The over-sampling factor (Sun et al. 2007) $f_{\text{oversample}}$ can be evaluated by

$$f_{\text{oversample}} = \frac{p_{\text{moon}}}{T_{\text{scan}}\, v_{\text{track}}}, \tag{18}$$

where p_{moon} is the pixel size of the detector on the lunar surface, T_{scan} is the time of one scan, and v_{track} is the projection of the velocity of the detector on the lunar surface along the track direction. The time T_{moon} of one IFOV along the track direction is

$$T_{\text{moon}} = \frac{p_{\text{moon}}}{v_{\text{track}}}. \tag{19}$$

The Equation (19) is substituted into Equation (18), and the over-sampling factor $f_{\text{oversample}}$ is

$$f_{\text{oversample}} = \frac{T_{\text{scan}}}{T_{\text{moon}}}. \tag{20}$$

The time T_{scan} of one scan for the imaging spectrometer is

$$\begin{aligned} T_{\text{scan}} &= T_{\text{integration}} + T_{\text{shift}} \quad T_{\text{shift}} \\ &= \begin{cases} 0.0113 & T_{\text{integration}} \geqslant 0.873 \text{ s} \\ 0.9788 & T_{\text{integration}} \leqslant 0.874 \text{ s} \end{cases}, \end{aligned} \tag{21}$$

where $T_{\text{integration}}$ is the integration time of the imaging spectrometer, and T_{shift} is the CCD frame transfer time related to $T_{\text{integration}}$.

3.2.5. Spatial Resolution

The pixel numbers N_{moon} in spatial dimension for the Moon (approximately $0^{\circ}.5$) is expressed by

$$N_{\text{moon}} = \frac{T_{\text{disk}}}{T_{\text{scan}}} = \frac{T_{\text{disk}}}{f_{\text{oversample}}\, T_{\text{moon}}} = \frac{\Omega_{\text{moon}}}{f_{\text{oversample}}\, \psi_{\text{instantaneous}}}. \tag{22}$$

To maintain the same spatial resolution lunar imaging as far as possible in one night, N_{moon} should be a constant, which is determined by the over-sampling factor and the IFOV in Equation (22). As long as the same over-sampling factor is used for the whole night, a uniform spatial resolution can be maintained for splice images in the along-track direction. The Equation (21) is substituted into Equation (20), and the integration time $T_{\text{integration}}$ is

$$T_{\text{integration}} = f_{\text{oversample}}\, T_{\text{moon}} - T_{\text{shift}}. \tag{23}$$

The integration time $T_{\text{integration}}$ can be determined by the over-sampling factor and angular velocity, and which is calculated by the current clock time $T + n\Delta T$ in Figure 7.

The integration time ($f_{\text{oversample}} = 1$) and the angular velocity with time from 2015 December 18 to 2016 January 3, which are respectively determined by the Equations (23) (5), are shown in Figure 8. When $\theta_{\text{lunar}} < \theta_{\text{threshold}}$ ($\theta_{\text{threshold}} = 90^{\circ}$), the solid lines are similarly a parabola from moonrise to moonset. The light-green lines show the case of $\theta_{\text{Sun}} > 108^{\circ}$ and $\theta_{\text{lunar}} < \theta_{\text{threshold}}$. The red lines represent integration time of the observation time determined by the Equation (15), and the blue lines show the angular velocity for the observation time determined by Equation (15). When the Moon is at meridian,

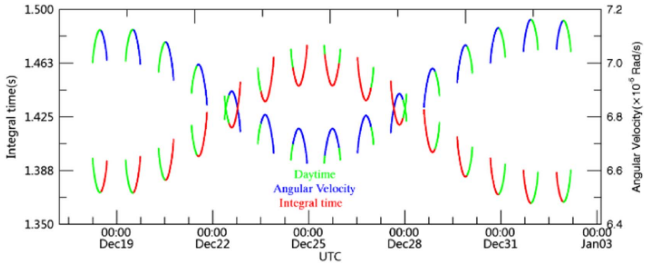

Figure 8. Integration time and angular velocity with time from 2015 December 18 to 2016 January 3.
(A color version of this figure is available in the online journal.)

the integration time is a minimum value, and the angular velocity of the Moon is a maximum value. In Figure 8, the apparent angular velocity of the full Moon is less than that of the other Moon phase, and the variation in the integration time ($f_{\text{oversample}} = 1$) at phase angles -90°–90° is about 8%.

To set the integration time $T_{\text{integration}}$, the oversampling factor $f_{\text{oversample}}$ should be obtained in Equation (23). The Equation (21) is substituted into Equation (20). At the beginning of all the lunar observations, the over-sampling factor $f_{\text{oversample}}$ is

$$f_{\text{oversample}} = \frac{T_{\text{integration}}(t_0) + T_{\text{shift}}}{T_{\text{moon}}(t_0)}, \tag{24}$$

where t_0 is the initial time in Equation (15), which the Moon starts to be observed in one night.

The over-sampling factor $f_{\text{oversample}}$ is a function of $T_{\text{integration}}$ and T_{moon}. The Equation (24) is substituted into Equation (23). Since the pointing position of the mount is fixed in one night, the integration time $T_{\text{integration}}(t_n)$ at lunar observation time t_n is

$$T_{\text{integration}}(t_n) = \frac{T_{\text{integration}}(t_0) + T_{\text{shift}}}{T_{\text{moon}}(t_0)} T_{\text{moon}}(t_n) - T_{\text{shift}}. \tag{25}$$

The time $T_{\text{moon}}(t_n)$ at any observation time t_n and the time T_{shift} for the frame-transfer CCD are well known. As long as the integration time $T_{\text{integration}}(t_0)$ is given in Equation (25), the hyper-spectral imaging cube is automated in a uniform spatial resolution.

3.2.6. Integration Time Setting

In Equations (22) and (25), each scanning line of the Moon should keep similar spatial resolution in along-track direction for one night, so the integration time $T_{\text{integration}}(t_0)$ need to be set for the same oversampling factor. To gain a high S/N performance in the linear zone of the CCD detector, the integration time $T_{\text{integration}}(t_0)$ should be in a rational range. The lunar radiance is one important factor for determining the integration time of instruments, so the integration time $T_{\text{integration}}(t_0)$ is mainly determined by the maximum observation radiance $L_{\text{obs,max}}$ of the hyper-spectral image cube in

Equation (26):

$$L_{\mathrm{obs,max}} = T_{\mathrm{atm}} \max(L_{\theta}^{\mathrm{TOA}}) = R \times DN_{\max} T_{\mathrm{integration}} \quad (DN_{\max} \leqslant DN_0), \tag{26}$$

where T_{atm} is the atmospheric transmission, $DN_{\max}$ is the maximum digital number of the hyper-spectral image cube, DN_0 is the maximum digital number in the linear zone of the CCD detector, R is a constant for the imaging spectrometer, and $L_{\theta}^{\mathrm{TOA}}$ is a hyper-spectral image cube at the zenith angle of θ, which is the top-of-atmosphere radiance with respect to the Moon-Earth distance, the Moon-Sun distance and the lunar angle.

The atmospheric transmittance T_{atm} is

$$T_{\mathrm{atm}} = e^{-m(\theta)\tau}, \tag{27}$$

$$m = [\cos\theta + 0.15(93.885 - \theta)^{-1.253}]^{-1} \times \frac{P(z)}{P_0}, \tag{28}$$

where m is the air mass of the Moon, τ is the optical depth of total atmosphere at the observational daytime, θ is the lunar zenith angle range in Equation (14), $P(z)$ is the atmospheric pressure of the observation site, and $P_0 = 1013$ h pa.

When $DN_{\max} = DN_0$, the minimum integration time $T_{\mathrm{integration}}(\theta)$ required for the zenith angle θ to enable the imaging spectrometer to observe the Moon in the linear zone of the CCD detector is

$$T_{\mathrm{integration}}^{\min}(\theta) = \frac{1}{R \times DN_0} T_{\mathrm{atm}}(\theta) \max(L_{\theta}^{\mathrm{TOA}}). \tag{29}$$

When the zenith angle θ is equal to the initial lunar zenith angle θ_0 at the beginning of all the lunar observations, the minimum integration time is

$$T_{\mathrm{integration}}^{\min}(\theta_0) = \frac{1}{R \times DN_0} T_{\mathrm{atm}}(\theta_0) \max(L_{\theta_0}^{\mathrm{TOA}}). \tag{30}$$

When the zenith angle θ is equal to the minimum lunar zenith angle $\theta_{\min}$ during one night in Equation (30), the minimum integration time is

$$T_{\mathrm{integration}}^{\min}(\theta_{\min}) = \frac{1}{R \times DN_0} T_{\mathrm{atm}}(\theta_{\min}) \max(L_{\theta_{\min}}^{\mathrm{TOA}}). \tag{31}$$

It is assumed that the maximum value of the lunar radiance $L_{\theta}^{\mathrm{TOA}}$ does not change with time during the whole night, so the minimum integration time $T_{\mathrm{integration}}^{\min}(\theta_{\min})$ based on Equations (30) and (31) is

$$T_{\mathrm{integration}}^{\min}(\theta_{\min}) \approx T_{\mathrm{integration}}^{\min}(\theta_0) \cdot e^{-(m(\theta_{\min}) - m(\theta_0))\tau}. \tag{32}$$

θ_0, $\theta_{\min}$, and τ are respectively provided by the SAMPA and the lunar-photometer CE-318U. $T_{\mathrm{integration}}^{\min}(\theta_0)$ is measured at the zenith angle of θ_0, so the minimum integration time $T_{\mathrm{integration}}^{\min}(\theta_{\min})$ can be calculated at the zenith angle of $\theta_{\min}$. In fact, the maximum value of the lunar radiance L^{TOA} as a function of phase angle has an approximately $\pm 4\%$ spread within 7 hour from the zenith angle $\theta_{\mathrm{threshold}}(90^\circ)$ to the zenith in Equation (33)

$$-4\% < \frac{\max(L_{\theta_{\min}}^{\mathrm{TOA}})}{\max(L_{\theta_0}^{\mathrm{TOA}})} < 4\%. \tag{33}$$

When the oversampling factor is equal to 1, the percentage change of the integration time $T_{\mathrm{integration}}^{\min}$ calculated in Equation (23) is about -1.5% from the zenith angle $\theta_{\mathrm{threshold}}$ to the zenith. Thus, the percentage change of the integration time is negligible during one night. To effectively maintain a better signal of the CCD detector, the integration time $T_{\mathrm{integration}}^{\min}(t_0)$ at time t_0 is approximately equal to the integration time $T_{\mathrm{integration}}^{\min}(\theta_{\min})$ at the zenith angle of $\theta_{\min}$

$$T_{\mathrm{integration}}(t_0) \approx T_{\mathrm{integration}}^{\min}(\theta_{\min}). \tag{34}$$

The integration time $T_{\mathrm{integration}}(t_0)$ at time t_0 is mainly determined by the atmospheric extinction, and acted as the integration time $T_{\mathrm{integration}}(t_0)$ in Equation (24). Therefore, hyper-spectral imaging data with high S/N is automatically obtained in a uniform spatial resolution.

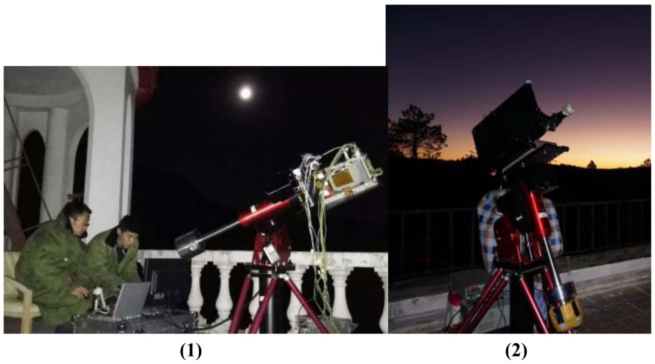

(1) (2)

Figure 9. Ground-based observation of the Moon. (1) Early testing observations in Lingshan Mountain, and (2) Formal observations viewed from Lijiang, Yunnan Province.
(A color version of this figure is available in the online journal.)

4. Lunar Observations and Preliminary Results

4.1. Experiment

4.1.1. Early Testing Observations

To validate the performance of the instrument design and the function of lunar observations, the ground-based observations of the Moon were conducted at Lingshan Mountain, Beijing from 2015 June to 2015 July. The experimental observations were also done at Yang guan town of Dun Huang city in 2015 August. The field observations of the Moon gave several important experiments for the observation schemes and the instrument design. In-situ observation photo at Lingshan Mountain is shown in Figure 9 (1), but these two places are

unsuitable for lunar observations for the lunar model establishment or improvement because of the atmosphere condition and low possibility of clear sky.

4.1.2. Formal Observations

A three-month series observations of the Moon using ground-based imaging spectrometer has been conducted formally at Lijiang Observatory, Yunnan (lat.26°45′40.″00 N, long.100°02′33.″00 E, alt.3175 m). The site of the observations is located at the peak of Mountain Gaomeigu, which is surrounded by pine forest and about 50 km away from Lijiang city. The air of the observation site is essentially free of aerosols, and the atmosphere condition of the observations in the night is excellent with less than 0.1 of aerosol optical depth at 0.55 μm in the most of days (L. Chen 2016, personal communication). The automated observations were made from first half Moon (Waxing Moon) to last half Moon (Waning Moon) of each month during 2015 December to 2016 February. The observation system was located on the balcony of a second floor of Lijiang weather Radar station which has a clear field of viewed to the Moon (see Figure 9(2)).

At the same time, data collected on-site by radiosonde balloons, LIDAR, lunar-photometer CE-318U, Sun-photometer CE-318 and atmospheric sounders were used to help with the acquisition of model parameters for atmospheric correction for lunar observations. During each observation, the optical depth of the atmosphere extinction was estimated using the Langley plot and Lunar-Langley methods (Langley 1881; Barreto et al. 2013) from the CE-318 data, which was obtained by observing the Sun and the Moon in nine bands (381, 340, 440, 500, 677, 870, 936, 1021 and 1643 nm). LIDAR system was also used to characterize the aerosol back scattering in the vertical path of the atmosphere. LIDAR, in particular, has great potential to help quantify atmospheric variability and homogeneity.

4.1.3. Absolute Calibration and Instrument Characterization

The imaging spectrometer was characterized and calibrated by the manufacture before lunar observation experiment. Laser-based methods were commonly used for spectral calibration, and the main advantages of which are very accurately known wavelengths and small bandwidth. To accurately calibrate the radiometric response, stray light outside the field of view of the instrument and spectral cross-talk were measured in the laboratory. And the smear effect and response difference of the CCD detector were obtained in the radiometric calibration process. After the Lijiang campaign, absolute calibration was conducted based on Chinese NIM radiance standard. Lamp-Plate system and low brightness integrating sphere were used for this absolute calibration with quartz-tungsten halogen lamps of known output values.

To monitor the running status of the imaging spectrometer, the characteristic spectrum lines of mercury lamp and the temperature of optical components were used to monitor the wavelength drift of the instrument. In addition, a spectralon reference panel was viewed simultaneously by the imaging spectrometer and a portable spectroradiometer ASD occasionally for monitoring radiometric response stability of the instrument. This kind of job was also checked on site using the integrating spheres measured at the same direction by both the instruments above.

4.2. Preliminary Results

To check the effectiveness of lunar observations, the raw data from lunar observations is first reduced to a full-disk irradiance. For the imaging spectrometer data, the data processing began with raw data apart from a "smear and dark current" correction which includes integration time normalization and oversampling correction. The disk-integrated irradiance $I(\lambda_k)$ is derived from the integration of lunar images that have not been corrected for atmospheric extinction

$$I(\lambda_k) = \frac{\Omega_p}{T_{\text{integral}} f_{\text{oversample}}} \sum_{i=1}^{N_{\text{track}}} \sum_{j=1}^{N_{\text{cross}}} R_{i,j}(\lambda_k), \tag{35}$$

where Ω_p is the solid angle of 1 pixel, R is an individual radiance measurement (i.e., pixel) and λ_k is the wavelength of band k, N_{track} is the pixel numbers along the track direction, N_{cross} is the pixel numbers in spatial dimension.

4.2.1. Result

In Figure 10, the Moon image (580 nm) of the imaging spectrometer and the Moon image of imaging monitor were acquired at 16:01:47 UTC on 2015 December 24 at a phase angle of −11.°46. For the imaging spectrometer, the oversampling factor of the raw image is 0.9439, and the raw image is reduced to a full-disk image using resampling methods. The comparison is made between the resampling image and the lunar image from the imaging monitor through using rotation and symmetry operation. It shows that the contours of the lunar images (right) for ① and ② are almost the same.

In Figure 11, the lunar image was obtained at 16:01:47 UTC on 2015 December 24, and the phase angle was −11.°46. The lunar images from the imaging spectrometer were obtained in the wavelength from 400 to 1000 nm. The spectral radiances from the hyper-spectral imaging cube are compared between bright spot and dark spot in Figure 11.

Lunar observations were performed for the two-week period each month between first and last quarter lunar phase from 2015 December to 2016 February. The 17-day effective measurements were conducted at cloud-free night, and the atmospheric conditions were relatively stable (see Figure 12). The lunar radiance images were obtained on these nights,

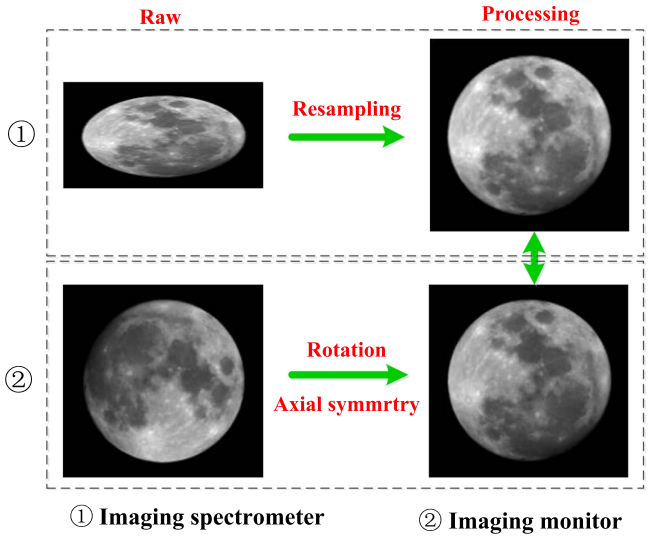

Figure 10. Lunar images comparison of the imaging spectrometer and imaging monitor. ① is from the imaging spectrometer and ② is from the imaging monitor.
(A color version of this figure is available in the online journal.)

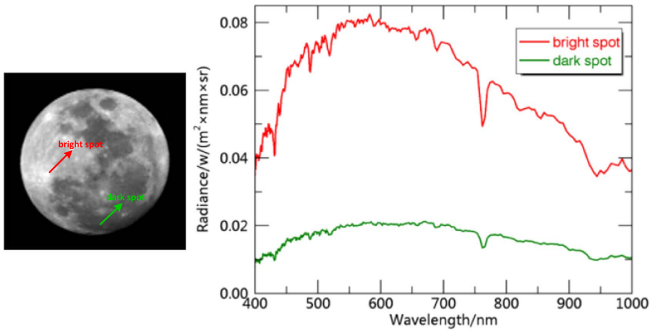

Figure 11. Spectral radiance comparison between bright spot and dark spot in the Moon image.
(A color version of this figure is available in the online journal.)

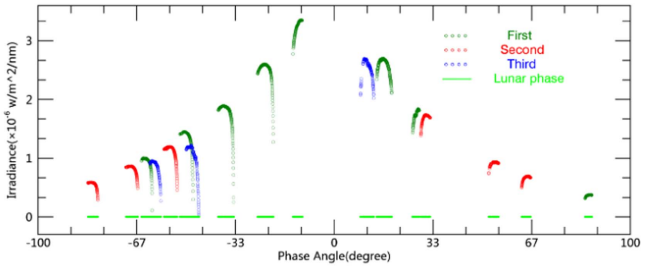

Figure 12. Observation disk-integrated irradiance with phase angle at 700 nm in Lijiang. Different line (First, Second, or Third) means the different lunar period from December to February.
(A color version of this figure is available in the online journal.)

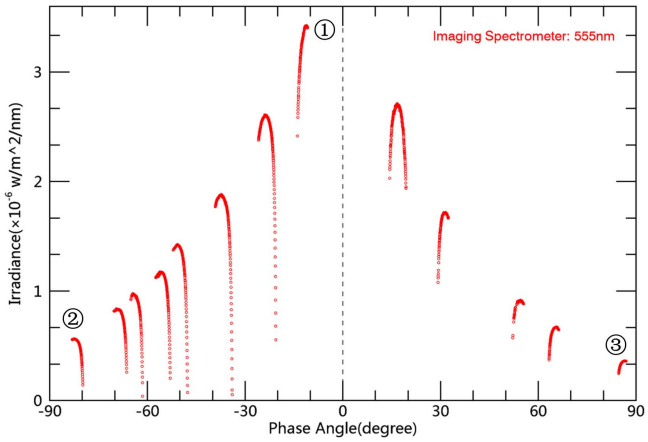

Figure 13. Ground-based observational irradiance of lunar disk in several days at Lijiang.
(A color version of this figure is available in the online journal.)

spanning phase angles from −83°.11 to 87°.27 and covering air masses from 1.10 to 5.76. Figure 12 shows the observed disk-integrated irradiance change at 700 nm as the Moon rises and sets, and as the Sun–Moon–Earth geometry changes throughout these nights. From these ground-based measurements without atmosphere correction, the lunar irradiances of three days (blue lines) with lunar phase show a little smaller in the third lunar phase period than the others, mostly owing to low atmospheric transparency with heavier aerosol loading. The light green lines in Figure 12 show the lunar phase range during the three-month observations, then it indicates the data is missing around the full Moon or so.

4.2.2. Relative Comparison

In Figure 13, the lunar images are reduced to the disk-integrated irradiance $I(\lambda_k)$ without atmosphere correction. The four-day measurements are removed because of the unstable atmosphere among all the observational days, and the 13-day measurements are plotted in Figure 13 at 555 nm. ① is $I(\lambda_k)$ of the observational day in transit time, which is approximately close to the full Moon, and ② and ③ represent the lunar irradiances in the zenith for the first quarter and third quarter, respectively.

It is assumed that the variation in the Earth–Moon distance and the Moon–Sun distance with time can be ignored. When the atmospheric extinction is thought to be same in transit time for all the observational days, the disk-integrated irradiance in Figure 13 is in proportion to the disk-equivalent reflectance (Kieffer & Stone 2005) at 555 nm from Figure 6 (Lunar disk reflectance versus phase angle). For the observational irradiance (Figure 13) and disk-equivalent reflectance of ROLO, the specific values of ① and ② are about 6, and the specific values of ① and ③ are about 9. It indicates small differences in the relative

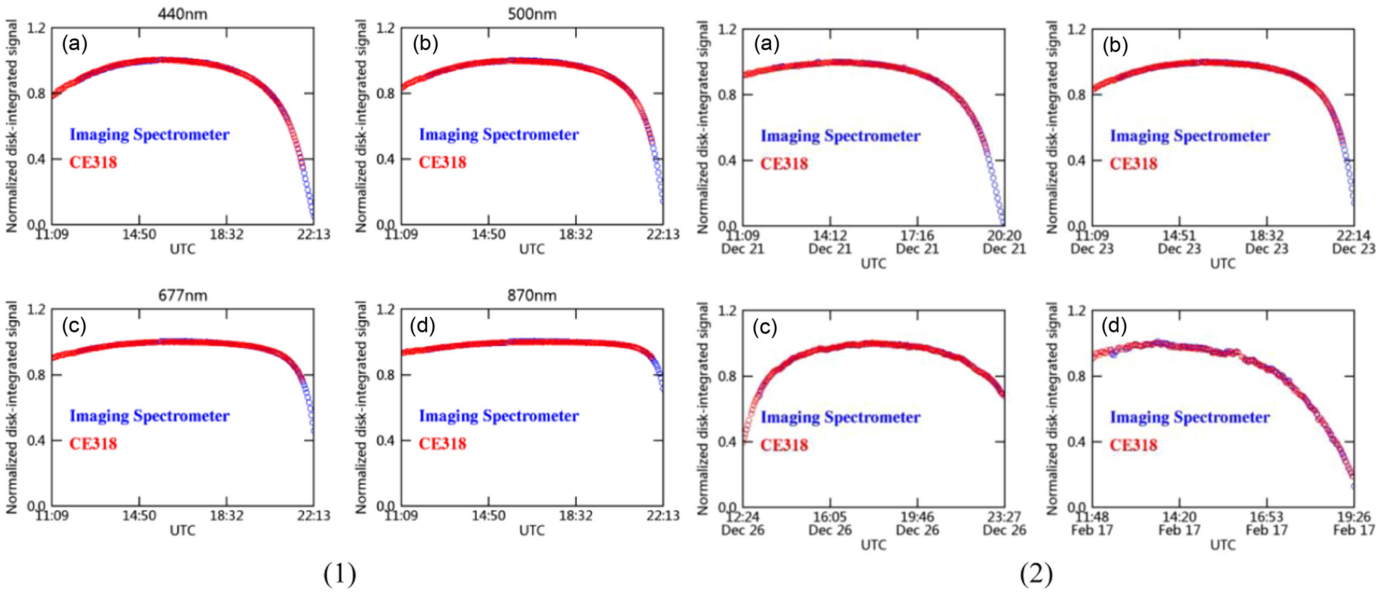

Figure 14. Lunar cross-comparison of CE-318U and imaging spectrometer (1) wavelength and (2) time.
(A color version of this figure is available in the online journal.)

variation with phase angle greatly due to the atmospheric extinction, but the variation tendency of disk-integrated irradiance with phase angle in Figure 13 is well consistent with ROLO Lunar Phase Function (Kieffer & Stone 2005)

In Figure 14(1), by comparing imaging spectrometer observations with lunar-photometer CE-318U observations in the same atmospheric path, the curves at 440 nm (a), 500 nm (b), 677 nm (c) and 870 nm (d) show a good agreement for normalized disk-integrated signals. In Figure 14(2), the relative trends of the disk-integrated signals for the imaging spectrometer and the CE-318U are generally in agreement at 500 nm on December 21 (a), December 23 (b), December 26 (c), and February 17 (d). The tendencies of these curves from the imaging spectrometer are well consistent with that from the lunar CE-318U in both the wavelength and time. The ground-based cross-comparison using the Moon between instruments shows that the validation of the instrument performance has been achieved, and it indicates the hyper spectral imaging data is also highly reliable.

5. Conclusion and Forward

We have developed a hyper-spectral, spatially resolved automated radiometric observation system of the Moon for lunar model improvement and validation in the calibration of Earth-observing instruments. A three-month observing campaign using this ground-based observation system for the entire lunar disk imaging was carried out in Lijiang city, Yunnan over a wide range of phase angles in the spectral range from 400 to 1000 nm. With the scanning scheme which the instrument does not move but the Moon moves, the tracking system is separated from observations using the imaging spectrometer to meet the requirements of the uncertainty in the tracking. The ground-based observation control system could accomplish automatically the observing process by adopting orbit prediction of the moving Moon and time bias. The simulation results show the feasibility of automated observation scheme, and the hyper-spectral imaging data with high S/N is automatically obtained in a uniform spatial resolution. Instrument performance and lunar observation capability are well checked by observational results and data comparison. Next, we will work on accurate spectral and radiometric calibration processing, atmospheric correction and complete comparison with the current lunar models. The accuracy of ground-based observations will be well improved by the further accumulation of observed data and often field accurate calibration for the instruments. The field experiences and remote control of this observation system will be also very useful for the instrument design and observation scheme in the future.

This paper was supported by National High-tech R&D 863 Program of China (2015AA123704), and the Special Scientific Research Fund of Meteorological Public Welfare Profession of China (grant no. 201506074). The authors thank Lin Chen, Ronghua Wu, and Lu Zhang of the National Satellite Meteorological Center, China for help in development of the ground-based observation and data reduction. Optical design of the imaging spectrometer was done by Qingsheng Xue at Changchun Institute of Optics, Fine Mechanics and Physics, Chinese Academy of Sciences, and operational procedures of the ground-based lunar observation system was provided by Weiping

Wu at CIOMP. The imaging spectrometer was characterized and calibrated by Anhui institute of optics and fine mechanics, China, and National Institute of Metrology, China. LIDAR is manufactured by the Beijing Research Institute of Telemetry.

References

Barnes, W. L., Eplee, J. R. E., Butler, J. J., et al. 2004, Proc. SPIE, 5542, 1
Barreto, A., Cuevas, E., Damiri, B., et al. 2013, AMT, 6, 585
Berkoff, T. A., Sorokin, M., Stone, T., et al. 2011, JAtOT, 28, 1297
Besse, S., Yokota, Y., Boardman, J., et al. 2013, Icar, 226, 127
Butler, J. J., Snow, M., Xiong, J., et al. 2007, Proc. SPIE, 6677, 66770D
Cramer, C. E., Fraser, G. T., Lykke, K. R., et al. 2013a, Proc. SPIE, 118, 641
Cramer, C. E., Lykke, K. R., Woodward, J. T., & Smith, A. W. 2013b, J Res Natl Inst Stand Technol, 118, 396
Gupta, R., & Hartley, R. I. 1994, ITPAM, 19, 555
Jr, E. R., Sun, J. Q., Meister, G., et al. 2011, ApOpt, 50, 120
Kieffer, H. H. 1997, Icar, 130, 323
Kieffer, H. H., & Anderson, J. M. 1998, Proc. SPIE, 3498, 325
Kieffer, H. H., & Stone, T. C. 2005, AJ, 129, 2887
Kieffer, H. H., & Wildey, R. L. 1996, JAtOT, 13, 360
Lane, A. P., & Irvine, W. M. 1973, AJ, 5, 293
Langley, S. P. 1881, Proc. Am. Acad. Arts Sci, 8, 343
Lawrence, S., Lau, E., Steutel, D., et al. 2003, in Lunar Planet. Sci. Conf. 34, A New Measurement of the Absolute Spectral Reflectance of the Moon (League City, TX: Lunar and Planetary Inst.), 1269
Miller, S. D., & Turner, R. E. 2009, ITGRS, 47, 2316
Ohring, G., Tansock, J., Emery, W., et al. 2007, EOSTr, 88, 136
Ohring, G., Wielicki, B., Spencer, R., et al. 2005, BAMS, 86, 1303
Ohtake, M., Pieters, C. M., Isaacson, P., et al. 2013, Icar, 226, 364
Pieters, C. M., Boardman, J. W., Ohtake, M., et al. 2013, Icar, 226, 951
Saiki, K., Saito, K., Okuno, H., et al. 2008, E&PS, 60, 417
Smith, A. W., Lorentz, S. R., Stone, T. C., & Datla, R. V. 2012, J Res Natl Inst Stand Technol, 117, 185
Sun, J. Q., Xiong, X., Barnes, W. L., & Guenther, B. 2007, ITGRS, 43, 2383
Velikodsky, Y. I., Opanasenko, N. V., Akimov, L. A., et al. 2011, Icar, 214, 30